# Ferromagnetic single-atom spin catalyst for boosting water splitting

*Tao Sun[1,9], Zhiyuan Tang[2,9], Wenjie Zang[3,9], Zejun Li[4], Jing Li[1], Zhihao Li[5], Liang Cao[5], Haomin Xu[1], Pin Lyu[1], Xiao Hai[1], Huihui Lin[1], Xiaoyu Sheng[1], Jiwei Shi[1], Yi Zheng[6], Qian He[3], Jingsheng Chen[3], Kostya S Novoselov[3,8], Shibo Xi[7*], Xin Luo[2*] and Jiong Lu[1,8*]*

[1]Department of Chemistry, National University of Singapore, 3 Science Drive 3, Singapore 117543, Singapore.

[2]State Key Laboratory of Optoelectronic Materials and Technologies, Guangdong Key Laboratory of Magnetoelectric Physics and Devices, Centre for Physical Mechanics and Biophysics, School of Physics, Sun Yat-sen University, Guangzhou 510275, China.

[3]Department of Materials Science and Engineering, Faculty of Engineering, National University of Singapore, 117574, Singapore.

[4]School of Physics, Frontiers Science Center for Mobile Information Communication and Security, Southeast University, Nanjing 211189, China.

[5]Anhui Province Key Laboratory of Condensed Matter Physics at Extreme Conditions, High Magnetic Field Laboratory, HFIPS, Chinese Academy of Sciences, Hefei 230031, China.

[6]Zhejiang Province Key Laboratory of Quantum Technology and Device, Department of Physics, Zhejiang University, Hangzhou 310058, China.

[7]Institute of Chemical and Engineering Sciences, 1 Pesek Road, Jurong Island, Singapore 627833, Singapore.

[8]Institute for Functional Intelligent Materials, National University of Singapore, 117544, Singapore.

[9]These authors contributed equally: Tao Sun, Zhiyuan Tang, Wenjie Zang.

[*]e-mail: xi_shibo@partner.nus.edu.sg; luox77@mail.sysu.edu.cn; chmluj@nus.edu.sg

**Abstract**

Accelerating chemical reactions by commonly accessible magnetic fields provides powerful knobs to enhance the overall reaction efficiency involving the spin change. However, the design of heterogeneous spin catalyst with atomically-precise active sites to boost reaction kinetics remains challenging as one must tackle multiple complexities including the ability to engineer well-defined active sites with the short-range quantum spin exchange interaction (QSEI) and long-range ferromagnetic ordering. Here, we devised a general and scalable approach for the synthesis of a new class of single-atom spin catalysts (SASCs) consisting of various substitutional magnetic atoms ($M_1$) in the $MoS_2$ host. Hydrothermal synthesis under acidic conditions allows to achieve isolated magnetic dopants with a widely tunable atomic doping ratio ($M_1$/Mo) up to ~20:100. All the SASCs exhibit interatomic QSEI to induce local magnetic moments with spin density delocalized over adjacent S atoms *via* strong *p-d* orbital hybridization. $M_1/MoS_2$ SASCs ($Mn_1$, $Fe_1$, $Co_1$) adopt trigonal prismatic geometries, while $Ni_1/MoS_2$ exhibits distorted tetragonal structure with local ferromagnetic coupling between Ni and nearest S atoms, and global room-temperature ferromagnetism. Ferromagnetic coupling between Ni and nearest S atoms favors spin-selective charge transfer for oxygen evolution reactions (OER) that involves the splitting of water into triplet $O_2$. Moreover, a mild magnetic field of ~0.5 T over $Ni_1/MoS_2$ yields a maximum enhancement of OER magnetocurrent by ~2880%, revealing an excellent activity and stability in both seawater and pure water splitting cells, superior to commercial $IrO_2$. Such a giant magnetic field enhancement for $Ni_1/MoS_2$ can be attributed to the optimization of spin density over S active sites and ferromagnetic alignment of weakly coupled spin centers under mild magnetic fields that give rise to optimal adsorption energy for radical intermediate with reduced reaction barriers. Our work offers unprecedented opportunities to design non-precious metal based ferromagnetic SASCs for both water and saline water electrolyser technologies.

**Main**

World-wild interest in hydrogen production from water electrolysis with renewable electricity has surged in recent years, since a hydrogen-based economy represents one of the best energy

alternatives to the increasing concerns over carbon emissions and climate change[1-4]. However, the bottleneck for efficient hydrogen production *via* water electrolysis lies in the sluggish kinetics of oxygen evolution reaction (OER) with the utilization of scarce precious metal based electrocatalysts[4-6]. The sluggish OER kinetics can be attributed to a multiple electron transfer process with the formation of triplet-state molecular oxygen ( $\uparrow O=O \uparrow$ ) that involves the spin change[7,8]. Despite extensive efforts devoted, the design of efficient and robust non-precious-metal OER spin catalysis with an abundance of desired active sites for the optimization of the adsorption/desorption strength of oxygen intermediates is still recognized as a major challenge[9-14]. Moreover, OER spin catalysts may also boost reactions by a mild external magnetic field to further increase the overall efficiency for water splitting towards green $H_2$ production[11-14].

Nature has evolved excellent spin catalysis from abundant 3d-metals for photosynthesis and biochemical processes (e.g. bird's migration)[15-17], whose reaction kinetics over spin catalysis can be influenced by external magnetic field through changing the spin multiplicity of pre-reactional state and allowing the switch from spin forbidden into spin-allowed reaction pathways[13,18]. Inspired by this, heterogeneous OER electrocatalysts including ferromagnetic mix-metal oxide/metal have been developed to boost OER performance under external magnetic field[11-14,18-23]. These ferromagnetic OER catalysts often yield a mild enhancement of OER currents under the external magnetic field (typically lower than 200 %). In addition, the surface reconstruction of active sites in these materials during OER reaction makes it challenging to establish the structure-performance relationship[12-14,19]. To date, a fundamental understanding of magnetic field enhancement (MFE) to further improve the efficiency of water electrolysis has remained elusive due to the challenge in identification of well-defined active sites in these systems. Therefore, rational design of heterogeneous spin catalyst with atomically precise active sites, enabling giant MEF with maximized atom and energy efficiency, is highly desired to create industrially-relevant water splitting technologies. To realize this goal, one must tackle multiple challenges including the ability to engineer a high density of well-defined active sites with both short-range QSEI and long-range room-

temperature ferromagnetic ordering, as well as weakly-interacting spin centers that can be altered under commonly accessible magnetic fields (e.g. permeant magnets).

**Rational Design and Synthesis**

To tackle these challenges, we devised a general and scalable method for the synthesis of a series of single-atom spin catalysts (SASCs) consisting of substitutional magnetic atoms embedded in the $MoS_2$ host. $M_1/MoS_2$ SASCs with tunable metal content were synthesized *via* a well-designed hydrothermal approach by introducing different molecular precursors including metal salts ($M^{2+}$), ammonium molybdate tetrahydrate and thioacetamide in one step (see the experimental section for details). The decomposition of thioacetamide during hydrothermal reaction not only provides S sources for the formation of 2H-phase $MoS_2$ host but also creates the desired acidic environment to facilitate the synthesis of atomically dispersed single atoms embedded into the carrier lattice (**Fig. 1a**) *by* suppressing the formation of metallic nanoparticles. As a result, such a general synthetic protocol allows for the scalable synthesis of various $M_1/MoS_2$ SASCs ($M_1$=Mn, Fe, Ni, Co) with widely tunable atomic doping ratio ($M_1$/Mo) up to ~20:100 (Supplementary **Table 1**). Generally, high doping density shortens the averaged spacing between adjacent magnetic dopant sites to promote their magnetic exchange interaction into long-range magnetic order (**Fig. 1a**). Atomic dispersion of single magnetic dopants in $MoS_2$ with different loadings can be confirmed using different characterization techniques including X-ray absorption fine structure (XAFS), X-ray diffraction (XRD) analysis, Raman spectra and electron microscopy imaging (**Fig. 1b-f**, Extended Data **Fig. 1a-c** and Supplementary **Fig. 1-5**).

We will first present the detailed structural characterization of $Ni_1/MoS_2$ SASCs with ferromagnetism in contrast to other paramagnetic $M_1/MoS_2$ SASCs synthesized in this work. XAFS and high-angle annular dark-field scanning transmission electron microscopy (HAADF-STEM) imaging were used to further elucidate the coordination environment of Ni atoms in $Ni_1/MoS_2$. HAADF-STEM image resolves a characteristic triangular lattice of $Ni_1/MoS_2$ consisting of brighter and darker sites (red circled in **Fig. 1g**), which can be assigned to Mo and Ni atomic sites, respectively. A zoom-in HAADF-STEM image (**Fig. 1h**

and Extended Data **Fig. 1d**) further unveils that single Ni atom (marked by yellow circle) substitutes Mo atom in the host (denoted as $Ni_{Mo}$), consistent with the contrast observed in the simulated HAADF-STEM image of DFT-optimized $Ni_{Mo}$ structure (**Fig. 1i**). In addition, Ni K-edge Fourier transformed extended X-ray absorption fine structure (EXAFS) spectrum of $Ni_1/MoS_2$ reveals an absence of any feature associated with Ni–Ni and Ni–O bond but a prominent feature peaked at 1.779 Å[24,25], similar to that of commercial $NiS_2$, which can be associated with the Ni–S bonding (**Fig. 1d**). Ni–S bond length and coordination number were determined to be 2.27 ± 0.02Å and 4.3 ± 0.2 *via* a detailed EXAFS fitting (Table S2). Among all the proposed structures, DFT-relaxed $Ni_{Mo}$ consisting of Ni in the replacement of Mo coordinated with adjacent four S atoms (denoted as $NiS_4$) in a planar tetragonal configuration shows the best agreement between experimental X-ray Absorption Near Edge Structure (XANES) and simulated spectrum (**Fig. 1e**, Extended Data **Fig. 1e, 1f** and Supplementary **Fig. 6**). Unlike $Ni_1/MoS_2$, other substitutional dopants in $M_1/MoS_2$ (M = Mn, Fe and Co) are coordinated with six adjacent S atoms to form the trigonal prismatic $MS_6$ configuration (**Fig. 1b, 1c**, Supplementary **Fig. 7, 8**, Supplementary **Table 2**). Individual $NiS_4$ site in $MoS_2$ contains four Ni–S bonds, wherein the shortest Ni–S bond length is 2.285 Å. The quasi-planar tetracoordinate Ni dopant breaks the rotation symmetry in the trigonal prismatic configuration ($D_{3h}$) to form single $Ni_{Mo}$ site with quasi-plannar tetragonal structure ($C_{2v}$), leading to the increasing strength of crystal field and reduced level degeneracy (**Fig. 2f**, Extended Data **Fig. 2d**, Supplementary **Fig. 9**). Such a local bonding configuration of $Ni_{Mo}$ site yields a valence state of $Ni_{Mo}$(III), as evidenced by characteristic adsorption edge in soft XAS (Supplementary **Fig. 10**).

**Magnetic Property and OER Performance**

$Ni_{Mo}$(III) with a $C_{2v}$ symmetry is expected to yield unpaired 3*d* electron, leading to the formation of local magnetic moment around $Ni_{Mo}$ site and potentially creating long-range magnetic order in $Ni_1/MoS_2$ at increased doping density. To verify this, we performed both Electron Spin Resonance (ESR) spectra and Superconducting Quantum Interference Device (SQUID) measurements to probe the magnetism of $Ni_1/MoS_2$ sample with different metal loadings (**Fig. 2**). First, $Ni_1/MoS_2$ with the lowest Ni content of 0.05 wt% only reveals the

paramagnetism without long-range magnetic ordering (**Fig. 2b**). In contrast, ferromagnetism emerges in $Ni_1/MoS_2$ samples with increased Ni loading of 0.20, 0.38, 0.95, 1.42, 2.41, 3.12 and 4.20 wt%, whose saturated magnetization and coercivity increase monotonically as a function of Ni contents (**Fig. 2a-c**), similar to TMD materials doped by other metals[26-29]. We then conducted detailed characterizations of ferromagnetic properties of one representative $Ni_1/MoS_2$ with a metal loading of 3.12 wt%. Temperature-dependent ESR spectra of this $Ni_1/MoS_2$ acquired from 2 K to 300 K (**Fig. 2d**, Supplementary **Fig. 11**) reveal a characteristic line-shape feature at the magnetic field of ~335 mT, consistent with the expected absorption behavior of Ni(III) (Supplementary **Fig. 11**)[30,31]. In addition, the linewidth of the ESR signal of $Ni_1/MoS_2$ (Extended Data **Fig. 2a**), defined as the peak-to-peak distance decreases as a function of temperature, indicating the emergence of ferromagnetic order[32,33]. The ferromagnetism of $Ni_1/MoS_2$ is also reflected in the field-dependent magnetization measurements (M-H) acquired at different temperatures ranging from 50 to 300 K (**Fig. 2e**, Supplementary **Fig. 12**), revealing a clear hysteresis loop and a saturation magnetic field of ~5000 Oe. Unlike $Ni_1/MoS_2$, pure $MoS_2$ and other $M_1/MoS_2$ (M = Mn, Fe and Co) show the paramagnetism at room temperature (Supplementary **Fig. 13, 14**). All these observations confirm that a high doping density of Ni atoms leads to ferromagnetism in $Ni_1/MoS_2$, which may boost its OER performance under external magnetic field (B-field).

We then evaluated B-field dependent OER performance of ferromagnetic $Ni_1/MoS_2$ samples by performing linear scan voltammogram (LSV) and chronoamperometric response (CP) measurements in 1 M KOH electrolyte. It is noted that the current density (overpotential at 20 mA $cm^{-2}$) increases (decreases) from 3.52 to 64.19 mA $cm^{-2}$ at 1.6 V vs. RHE (from 465 to 174 mV) as B-field increases from zero to 502 mT (**Fig. 3a**). The enhanced OER performance can be directly visualized from more rigorous oxygen gas bubbling over the $Ni_1/MoS_2$ electrode under B-field (Inset of **Fig. 3a**, Supplementary **Fig. 15**). Upon the application of a B-field of 502 mT (**Fig. 3b**), OER current densities can be improved by 5 to 28 times at 1.7 and 1.55 V vs. RHE, respectively. The B-field enhanced current density and Tafel slope reaches a plateau above 502 mT, consistent with the saturation magnetic field

determined from the M-H curve. In addition, overpotentials at the current density of 40 mA $cm^{-2}$ decreases from 547 to 283 mV, and Tafel slopes also gradually decrease from 75 to 44 mV $dec^{-1}$ upon the increase of B-field from 0 to 502 mT (Extended Data **Fig. 3a**, Supplementary **Fig. 16**). A small reduction of overpotential can generate a rapid increase of the OER current density[34,35]. It is noted that the electrochemically active surface area (ECSA) shows a negligible change under B-field. All these results indicate that the giant MFE of the OER activity of $Ni_1/MoS_2$ results from the ferromagnetic spin alignment under mild B-field (**Fig. 2e**, Supplementary **Fig. 17, 18**).

Next, we carried out systematic experimental studies to probe the origin of the B-field enhanced OER activity. First, we found that OER current density after removing B-field does not immediately return its initial value with respect to $Ni_1/MoS_2$ under zero field (Extended Data **Fig. 3d, 3f**). The retention ratio of current density between B-field off and on gradually decreases from 92% to 54% at 1.6 V vs. RHE, when the applied B-field increases from 118 to 502 mT (Supplementary **Fig. 19**). In addition, OER activity also undergoes a slow decay and returns the initial status 4 hours after switching off the B-field (Extended Data **Fig. 3e**). Such a behavior in the evolution of OER activity between B-field on and off is presumably associated with the rotation of ferromagnetic domains, in accordance with the characteristics of the ferromagnetic alignment and relaxation between B-field on and off. The ferromagnetic domains tend to align with external magnetic field but it usually doesn't immediately return to the original randomized magnetization state, and retain some of the net magnetization due to the intrinsic spin exchange interactions after switching off B-field[36-38]. In addition, we also found that $Ni_1/MoS_2$ with a Ni content lower than 0.20 wt% exhibits a negligible MEF of OER (Extended Data **Fig. 3c**), presumably due to its low density of ferromagnetic domains. In addition, as-synthesized Mn, Co and Fe doped $MoS_2$ with paramagnetic behavior also show the independence of OER performance on B-field (Supplementary **Fig. 20**). Furthermore, the conductivity of both $Co_1/MoS_2$ and undoped $MoS_2$ can be improved upon the application of B-field but their OER current densities remain nearly unchanged, ruling out the role of improved conductivity in MFE of OER activity (Extended Data **Fig. 3b**, Supplementary **Fig. 20**). Although the ion transfer rate can be improved under magnetic field,

the intrinsic OER activity of catalyst is largely determined by its electronic structure of active sites[11,18]. Therefore, all these results point out that the ferromagnetic spin alignment can be attributed to the B-field enhanced OER activity over $Ni_1/MoS_2$ (**Fig. 3a**, Supplementary **Fig. 21-23**).

**Mechanistic insights into giant MFE for $Ni_1/MoS_2$**

We then performed DFT calculations to gain atomic-level understanding of the origin of ferromagnetism in $Ni_1/MoS_2$ and its B-field enhancement of OER performance. First, spin-polarized DFT calculations reveal the prescence of unpaired Ni 3*d* electron over $Ni_{Mo}$ and induced ferromagnetic spin polarization over nearby Mo and S atoms, yielding a net spin of ~ 1.610 μB for $Ni_{Mo}$ and its surrounding S and Mo atoms (defined as $Ni_{Mo}$-S-Mo region, **Fig. 2g**, Supplementary **Fig. 24, 25**). The ferromagnetic ground state of $Ni_{Mo}$-S-Mo arises from the spin exchange interactions of the itinerant electron in the region, which can be described from the Stoner criteria (Supplementary **Fig. 26-28**, Supplementary **Table 3, 4**). According to the ratio of Ni:Mo for ferromagentic $Ni_1/MoS_2$, we further construct a supercell of $Ni_2Mo_{14}S_{32}$ to calculate the magnetic ground states of two adjacent $Ni_{Mo}$ sites. Among all the possible configurations with different Ni-Ni seperation distances (Supplementary **Fig. 25**, Supplementary **Table 5**), the one with Ni-Ni distance of ~6.390 Å represents the most stable configuration due to its lowest formation energy. Importantly, our DFT calculations reveal that the ferromagnetic (FM) coupling between these two $Ni_{Mo}$ sites is favorable by 30.67 meV per Ni atom over the anti-ferromagnetic (AFM) coupling (**Fig. 2h, 2i**), consistent with the RT ferromangetism observed in experiment. The ferromagnetic ground state of $Ni_1/MoS_2$ is further reflected in the density of states (DOS) plot of $Ni_{Mo}$-S-Mo region that shows an asymmetric distribution of spin-up and spin-down electron densities near the Fermi level ($E_F$) (**Fig. 2j**). Specifically, spin-polarized states near $E_F$ are mainly from the $3d_{xz}/d_{yz}$ orbitals of Ni dopant, $3p_x/p_y$ orbitals of six nearest-neighboring S atoms, and $4d_{z2}$ orbitals of six nearest-neighboring Mo atoms as revealed in the projected density of states (PDOS) in **Fig. 2j**. The electron localized function (ELF) plot of $Ni_1/MoS_2$ demonstrates that the Ni dopants increase electron delocalization involving a large charge transfer with the surrounding S atoms, as further reflected from the Bader charge analysis (Extended Data **Fig. 2e**, Supplementary

**Table 6**). In order to accommodate the transfer electron of Ni with a specific direction of spin polarization, the highest half-filled $p_x/p_y$ orbitals of S toms will be occupied by two parallel spin polarized electrons due to the Hund rules, where the direction of spin polarization is opposite to that of the tranferred electrons. As a result, the direction of magnetic moment in the vincinal $Ni_{Mo}$-S-Mo region tends to align with the doped Ni atoms (Supplementary **Fig. 29**).

The key question that remains to be addressed lies in mechanistic insights into remarkable MFE of OER performance of $Ni_1/MoS_2$. We first used DFT calculations to identify the active site of individual $Ni_{Mo}$ site for OER. To facilitate the discussion, we label three types of nearest S atoms to individual $Ni_{Mo}$ site as $S_1$, $S_2$, $S_3$, which represents adjacent S atom with a Ni-S bond length of 2.521 Å, adjacent S atom with a Ni-S bond length of 2.285 Å, and nearby S atom located at the center of Mo prism, respectively (**Fig. 4a**). The adsorption of *OH over $S_1$ is energetically favorable by 0.475 eV, 0.715 eV, 1.703 eV, 1.809 eV compared to that over $S_2$, $S_3$, Ni and nearest Mo site, respectively. This suggests that $S_1$ site is the most favorable active site for OER, mainly due to the strong electronic interaction between $S_1$ and the *OH (**Fig. 4a**, Supplementary **Fig. 30**, Supplementary **Table 7**), as evidenced by the large electron difference density, the dominant electron states at $E_F$ and the largest localized potential of $S_1$ among all three types of S atoms (**Fig. 4b**, Supplementary **Fig. 29, 31**). As a result, more charge transfer to the *OH facilitates the occurrence of the first step of OER process (**Fig. 4b**), which can greatly improve the intrinsic activity of OER over S atoms.

An increase of B field increases total magnetic polarization and the density of aligned magnetic moments from neighboring $Ni_{Mo}$ sites. To mimic this picture, we calculated the OER energy profiles over two neighboring $Ni_{Mo}$ sites under two representative magnetic configurations including ferromagnetic (FM) and antiferromagnetic (AFM) ordering (**Fig. 4d**, Extended Data **Fig. 4a**). FM-coupled active site exhibits a lower energy barrier of 0.315 eV in the rate-limiting step of OER (from *OOH to $O_2$ process), compared to AFM-coupled active sites with a higher energy barrier of 0.387 eV (**Fig. 4d**). As shown in **Fig. 4c**, the near-Fermi level spin density of $S_1$ of two FM-coupled $Ni_{Mo}$ sites is significantly reduced, as

compared to that of AFM-coupled counterparts. Therefore, the reduction of energy barrier in FM configuration can be attributed to the optimization of spin density over S active sites upon spin alignment under mild magnetic field, which give rises to the optimal adsorption energy for radical intermediate with reduced reaction barrier. Meanwhile, it is also found that the spin density of *OH and *O species exhibits the parallel alignment over $S_1$ and $S_2$ sites in the FM configuration, but shows the antiparallel spin alignment in the AFM configuration (**Fig. 4e**, **4f**). Therefore, the desorption of *OH and *O to form spin-triplet state $O_2$ over FM coupled $NiS_4$ sites is energetically more favorable by 0.072 eV than that on the AFM coupled sites, leading to a lower energy barrier of $O_2$ formation. It is noted that current OER reaction profile is the one with the lowest barrier as compared with other reaction paths (Supplementary **Fig. 32, 33**, Supplementary **Table 8**). In addition, we also considered another OER pathway involving the formation of a bridge-type O-H-O intermediate and evaluated the corresponding OER energy profile (Extended Data **Fig. 4a**). The FM-coupled configuration shows a superior OER activity with an energy barrier of 0.418 eV in the rate-limiting step of *OOH to $O_2$, lower than that of AFM-coupled configuration (0.668 eV). Similarly, two O atoms in *OOH species show the parallel spin alignment over FM-coupled active sites, whereas anti-parallel spin alignment of *OOH over AFM coupled active sites doesn't favor the *OOH desorption (Extend Data **Fig. 4b, 4c**).

**MFE for water splitting using $Ni_1/MoS_2$**

After gaining new insights into the mechanism of MFE of OER performance of $Ni_1/MoS_2$, we also tested its technological relevance by evaluating B-field dependent electrocatalytic performance in both water and seawater splitting cells. $Ni_1/MoS_2$ (3.12 wt%) also presents an outstanding OER performance under B-field for water splitting, much superior to commercial $IrO_2$ (**Fig. 3c**, Supplementary **Fig. 34**). The current density of $Ni_1/MoS_2$ at 502 mT is determined to be ~ 5.2-11.7 times higher than that under zero-B field in the potential range of 1.5-1.8 V. Moreover, $Ni_1/MoS_2$ at 502 mT also presents a high stability with a minor current density drop from 39.8 to 38.4 mA $cm^{-2}$ within 25 h, in contrast to commercial $IrO_2$ catalyst with a large current density decrease from 17.8 to 8.7 mA $cm^{-2}$ within the same period (**Fig. 3d**). In addition, $Ni_1/MoS_2$ (3.12 wt%) also reveals a remarkably improved OER performance

at 502 mT for seawater splitting, much better than commercial $IrO_2$ in terms of current density in a wide potential range of 1.5-1.8 V (**Fig. 3e**, Supplementary **Fig. 35**). Seawater splitting is recognized as a more economically-vital water splitting technology. However, the catalyst instability due to the presence of a variety of components in seawater, especially chloride ions[39,40], poses a great challenge for the practical utilization of seawater in water splitting technology. Commercial $IrO_2$ catalyst shows a rapid decay and drops in current density by 19.2 mA $cm^{-2}$ within 25 h. In contrast, $Ni_1/MoS_2$ demonstrates a negligible decrease in current density by 2.3 mA $cm^{-2}$ within the same period, revealing an excellent OER stability in seawater. This is likely due to a high tolerance of $Ni_1/MoS_2$ to the Cl adsorption against the catalyst deactivation (**Fig. 3f**, Supplementary **Fig. 36**, Supplementary **Table 10**), corroborated by our DFT calculations (Supplementary **Fig. 37, 38**). A large cell with an electrode (6 cm x 7 cm) loading $Ni_1/MoS_2$ exhibits a promising application in water splitting technology (Extended Data **Fig. 5**)

## Discussion

In summary, we have demonstrated a general and scalable approach for the synthesis of a series of SASCs ($M_1/MoS_2$) with widely tunable loadings. High-loading $Ni_1/MoS_2$ also exhibits the room–temperature ferromagnetism arising from the ferromagnetic coupling between adjacent $NiS_4$ sites embedded in $MoS_2$ lattice, offering a giant MFE of OER activity. In the water splitting cells, $Ni_1/MoS_2$ delivers an excellent catalytic performance with a large current density under magnetic field up to 502 mT, approximately one order of magnitude higher than that without applying magnetic field in 1.5-1.8 V, outperforming the commercial $IrO_2$ catalyst. A large B-field enhancement of OER performance of $Ni_1/MoS_2$ is attributed to their weakly coupled spin centers and the optimization of spin density over S active sites upon spin alignment under mild magnetic fields, which yields the optimal adsorption/desorption energy for radical intermediate with reduced reaction barrier, as corroborated by our DFT calculations. In addition, the stability of $Ni_1/MoS_2$ as OER catalyst is also superior to that of $IrO_2$ in pure water and seawater splitting cell, demonstrating its great potential in practical seawater splitting technology. Our findings reveal that

ferromagnetic SASCs provide a powerful magnetoelectric effect to accelerate both water and saline water electrolysis.

## Methods

**Synthesis of $M_1/MoS_2$ catalysts** A series of $M_1/MoS_2$ SASCs were prepared according to the designed synthetic protocol as follows. 176 mg $(NH_4)_6Mo_7O_{24}\cdot 4H_2O$ ($n_{Mo}$=1 mmol), a certain amount of metal salts ($Mn(CH_3COO)_2\cdot 4H_2O$, $Fe(CH_3COO)_2\cdot 4H_2O$, $Co(CH_3COO)_2\cdot 4H_2O$ and $Ni(CH_3COO)_2\cdot 4H_2O$) and 750 mg $CH_3CSNH_2$ (10.0 mmol) were dissolved in 70 ml distilled water. The solution containing precursors was then transferred into a Teflon-lined autoclave (100 ml). Subsequently, it was sealed and maintained at 180 °C for 20 h and then naturally cooled to room temperature. The resulting product was washed with distilled water and absolute ethanol for several times, and dried under vacuum at 60 °C for 12 h. Under the Ar flow of 100 sccm, the dried product was heated to 400 °C at a rate of 10 °C $min^{-1}$ and kept there for 2 hours in a furance, then cooled down to room temperature. A series of $M_1/MoS_2$ SASCs can be obtained using this approach by tuning the contents and types of metal salt precursors ($n_M$:$n_{Mo\ max}$=20 at%).

**Electrochemical measurements** The OER measurments including cyclic voltammetry (CV) and linear sweep voltammetry (LSV) polarization curves were performed using a CHI 760D workstation (CH Instruments) with the counter electrode of graphite rod (diameter 5 mm, 99.999%) and the reference electrode of $Hg/Hg_2Cl_2$ (saturated KCl). The electrochemical impedance spectroscopy (EIS) was carried out in the frequency range of 0.01 Hz to 100000 Hz. All the potentials were calibrated to the reversible hydrogen electrode (RHE), $E_{RHE} = E_{ref} + 0.059pH + 0.241$. $E_{ref}$ is the experimental potential measured against the $Hg/Hg_2Cl_2$ reference electrode, and 0.241 is the standard potential of $Hg/Hg_2Cl_2$ at 25 °C[41,42].

**Electrode fabrication** A piece of copper (Cu) foam was sonicated in acetone, ethanol and distilled water for several minutes, prior to the preparation of the electrode. 15 mg $MoS_2$-based catalyst was added into a mixture of 0.90 mL of ethanol and 100 μL of Nafion (Dupont®, 5 wt%) with 1 h ultrasonic treatment. 100 μL of fresh catalyst ink was dropped

onto a Cu foam (0.5×2 cm, catalysts are covered with 0.5 $cm^2$, *i.e.*, 0.5×1 cm), and dried at room temperature for 12 h. All tests were performed in 1.0 M KOH solution saturated with oxygen gas ($O_2$). For comparison, 10 mg $IrO_2$ catalyst was added into a mixture of 0.90 mL of ethanol and 100 μL of Nafion with 1 h ultrasonic treatment. 100 μL of fresh catalyst ink was dropped onto a Cu foam, and the loading of $IrO_2$ on Cu foam is 1 mg $cm^{-2}$. The samples were run 10 cycles to reach a steady state. The LSV measurements for $MoS_2$ and $IrO_2$ catalysts were recorded in $O_2$-saturated electrolyte at a scan rate of 5 mV $s^{-1}$. CV curves were recorded from 0.37 to 0.57 V vs. RHE with a scan rate of 10 mV $s^{-1}$ to 120 mV $s^{-1}$ to measure the electrochemical double-layer ($C_{dl}$) capacitance. The long-term stability was measured by chronoamperometric (CP) response under magnetic stirring. OER performances under different magnetic field were performed by tuning the distances between the electrode and magnets. Seawater was collected from Sentosa beach (Singapore), and filtrated by filter paper.

The Cu foil loaded with the catalyst (0.2 mg $cm^{-2}$) acts as the work electrode (anode), and the Pt wire is the cathode. 10 neodymium magnets (one magnet: 3 cm × 2 cm × 0.5 cm) were stacked and palced near the anode of water splitting cell. The magnetic field experienced by electrode was carefully calibrated using Gauss meter (TD8620, Shenzhen, China) (Supplementary **Fig. 39)**. A large water splitting cell was constructed using the two 6 cm × 10 cm carbon papers loaded with $Ni_1/MoS_2$ (3 mg $cm^{-2}$, 6 cm × 7 cm) and Pt/C (20 wt% Pt, 3 mg $cm^{-2}$, 6 cm × 7 cm) as anode and cathode respectively. 100 neodymium magnets (3 cm × 2 cm × 0.5 cm) were compiled into a large magnet and placed near anode.

**DFT calculations**

The first-principle calculations were performed by using density functional theory (DFT) implement in the Vienna *ab initio* simulation package (VASP)[43-45]. The electron exchange and correction were calculated with the generalized gradient approximation (GGA) in the parametrization of Perdew-Burke-Ernzerhof (PBE)[46] pseudopotentials including Hubbard-U corrections (DFT+U formalism) based on Dudarev's approach[47]. The projector augmented wave method with a plane-wave cutoff of 500 eV was used. The electronic states of $4d^5 5s^1$,

$3s^2 3p^4$, $3p^6 3d^8 4s^2$, $2p^2 2p^4$, $1s^1$ were treated as valence states for Mo, S, Ni, O and H atoms, respectively. According to the experimental Ni loading concentration, the $4 \times 4 \times 1$ supercell of $MoS_2$ with one Mo atom replaced by Ni atom was used to simulate the doping effect. A vacuum slab of 16 Å is added to avoid the interlayer interaction. The structures were relaxed with $2 \times 2 \times 1$ Gamma-centered k-points mesh for the supercell, and the electronic self-consistent calculations were performed using the $5 \times 5 \times 1$ k-points mesh. The relaxation is considered to be converged if the Hellmann-Feynman forced is less than 0.01 eV/Å, and the energy convergence is set as $10^{-7}$ eV for all calculations with a Gaussian smearing of 0.05 eV. The gas-phase $O_2$ and $H_2O$ were performed in a cubic box with the lattice constant of 15 Å using a single gamma k-point. To consider the strong electron correlation effect, a $U_{eff}$ = 2.5 eV was assigned to 3d electrons for Ni atoms[48,49].

The charge transfer was analyzed by the Bader charge with grid of $384 \times 384 \times 480$[50]. The differential electron density (DED) was also implemented to analyze the charge transfers during adsorption process. The DED was attained by formula:

$$\Delta\rho = \rho_{AB} - \rho_A - \rho_B$$

where $\rho_{AB}$ represents charge density of the whole system after absorption, $\rho_A$ and $\rho_B$ represent charge densities of adsorded species and catalyst, respectively.

**Acknowledgments**

J. Lu acknowledges the support from MOE Tier 2 (MOE2019-T2-2-044 and MOE-T2EP50121-0008) and MOE (Singapore) through the Research Centre of Excellence program (grant EDUN C-33-18-279-V12,I-FIM). X.L. acknowledges the support from the National Natural Science Foundation of China (12172386 and 12132020) and National Natural Science Foundation of Guangdong Province, China (2021B1515020021). Q. H. would like to acknowledge the support by National Research Foundation (NRF) Singapore, under its NRF Fellowship (NRF-NRFF11-2019-0002). A portion of this work was performed on the Steady High Magnetic Field Facilities, High Magnetic Field Laboratory, CAS.

## Author contributions

T.S. and J.L. conceived and designed the experiments. W.J.Z., H.M.X. and Q.H. performed the electron microscopy experiments and data analysis. T.S. performed materials synthesis and OER test. Z.H.L. and L.C. performed ESR spectra and analysis. J.L., X.H. and P.L. performed the Raman spectra and XAS analysis. J.W.S. and H.H.L. performed photos of large cell. S.B.X. performed the XAFS measurement and XANES simulations. H.H.L. and X.Y.S. performed the XRD measurement. Y.Z., J.S.C. and K.S.N. participated in discussion and analysis. Z.Y.T. and X.L. carried out theoretical calculations. T.S., Z.Y.T., X.L. and J.L. wrote the manuscript. All authors discussed and commented on the manuscript.

## Competing interests

The authors declare no competing interest.

## References


1. Seh, Z. W. *et al*. Combining theory and experiment in electrocatalysis: insights into materials design. *Science* **355**, eaad4998 (2017).
2. Glenk, G. *et al*. Economics of converting renewable power to hydrogen. *Nat. Energy* **4**, 216-222 (2019).
3. Davis, S. J. *et al*. Net-zero emissions energy systems. *Science* **360**, eaas9793 (2018).
4. Tong, W. M. *et al*. Electrolysis of low-grade and saline surface water. *Nat. Energy* **5**, 367-377 (2020).
5. Song, F. *et al*. Transition metal oxides as electrocatalysts for the oxygen evolution reaction in alkaline solutions: an application-inspired renaissance. *J. Am. Chem. Soc*. **140**, 7748-7759 (2018).
6. Sun, T. *et al*. Design of local atomic environments in single-atom electrocatalysts for renewable energy conversions. *Adv. Mater*. **33**, 2003073 (2021).
7. Gracia, J. Spin dependent interactions catalyse the oxygen electrochemistry. *Phys. Chem. Chem. Phys.* **19**, 20451-20456 (2017).
8. Gracia, J. *et al*. Principles determining the activity of magnetic oxides for electron transfer reactions. *J. Catal*. **361**, 331-338 (2018).
9. Zhang, Y. Y. *et al*. Recent advances in magnetic field-enhanced electrocatalysis. *ACS Appl. Energy Mater*. **3**, 10303-10316 (2020).
10. Li, X. N. *et al*. Optimized electronic configuration to improve the surface absorption and bulk conductivity for enhanced oxygen evolution reaction. *J. Am. Chem. Soc*. **141**, 3121-3128 (2019).

11. Ren, X. *et al*. Spin-polarized oxygen evolution reaction under magnetic field. *Nat. Commun*. **12**, 2608 (2021).
12. Yan, J. H. *et al*. Direct magnetic reinforcement of electrocatalytic ORR/OER with electromagnetic induction of magnetic catalysts. *Adv. Mater*. **33**, 2007525 (2021).
13. Wu, T. Z. *et al*. Spin pinning effect to reconstructed oxyhydroxide layer on ferromagnetic oxides for enhanced water oxidation. *Nat. Commun*. **12**, 3634 (2021).
14. Zhou, G. *et al*. Spin-sate reconfiguration induced by alternating magnetic field for efficient oxygen evolution reaction. *Nat. Commun*. **12**, 4827 (2021).
15. Buchachenko, A. L. *et al*. Electron spin catalysis. *Chem. Rev*. **102**, 603-612 (2002).
16. Naaman, R. *et al*. Chiral molecules and the electron spin. *Nat. Rev. Chem*. **3**, 250-260 (2019).
17. McCusker, J. M. Elelectronic structure in the transition metal block and its implications for light harvesting. *Science* **363**, 484-488 (2019)
18. Garcés-Pineda, F. A. *et al*. Direct magnetic enhancement of electrocatalytic water oxidation in alkaline media, *Nat. Energy* **4**, 519-525 (2019).
19. Chen, R. R. *et al*. $SmCo_5$ with a reconstructed oxyhydroxide surface for spin-selective water oxidation at elevated temperature. *Angew. Chem. Int. Ed*. **60**, 25884-25890 (2021).
20. Hunt, C. *et al*. Quantification of the effect of an external magnetic field on water oxidation with cobalt oxide anodes. *J. Am. Chem. Soc*. **144**, 733-739 (2022).
21. Zhang, Z. M. *et al*. Significant change of metal cations in geometric sites by magnetic-field annealing $FeCo_2O_4$ for enhanced oxygen catalytic activity. *Small* **18**, 210418 (2022).
22. Zhang, Y. Y. *et al*. Magnetic field assisted electrocatalytic oxygen evolution reaction of nickel-based materials. *J. Mater. Chem. A* **10**, 1760-1767 (2020).
23. Niether, C. *et al*. Improved water electrolysis using magnetic heating of FeC-Ni core-shell nanoparticles. *Nat. Energy* **3**, 476-483 (2018).
24. X. Hai, et al. Scalable two-step annealing method for preparing ultra-high-density single-atom catalyst libraries. *Nat. Nanotechnol*. **17**, 174-181 (2022).
25. Zhang, H. B. *et al*. Surface modulation of hierarchical $MoS_2$ nanosheets by Ni single atoms for enhanced electrocatalytic hydrogen evolution. *Adv. Funct. Mater*. **28**, 1807086 (2018).
26. Li, J. F. *et al*. Robust ferromagnetism in Cr-doped $ReS_2$ nanosheets demonstrated by experiments and density functional theory calculations. *Nanotechnology* **31**, 175702 (2020).
27. Zhang, F. *et al*. Monolayer vanadium-doped tungsten disulfide: a room-temperature dilute magnetic semiconductor. *Adv. Sci*. **7**, 2001174 (2020).
28. Ahmed, S. *et al*. High coercivity and magnetization in $WSe_2$ by codoping Co and Nb. *Small* **16**, 1903173 (2020).
29. Ahmed, S. *et al*. Colossal magnetization and giant coercivity in ion-implanted (Nb and Co) $MoS_2$ crystals. *ACS Appl. Mater. Interfaces* **12**, 58140-58148 (2020).
30. Zhecheva, E. *et al*. EPR analysis of the local structure of $Ni^{3+}$ ions in Ni-based electrode materials obtained under high-pressure. *J. Mater. Sci*. **42**, 3343-3348 (2007).
31. Wongnate, T. *et al*. The radical mechanism of biological methane synthesis by methylcoenzyme M reductase. *Science* **352**, 6288 (2016).

32. Krellner, C. *et al*. Relevance of ferromagnetic correlations for the electron spin resonance in Kondo Lattice systems. *Phys. Rev. Lett*. **100**, 066401 (2008).
33. Yahya, M. *et al*. ESR studies of transition from ferromagnetism to superparamagnetism in nano-ferromagnet $La_{0.8}Sr_{0.2}MnO_3$. *J. Magn. Magn. Mater.* **466**, 341-350 (2018).
34. Wu, Z. P. *et al*. Non-noble-metal-based electrocatalysts toward the oxygen evolution reaction. *Adv. Funct. Mater*. **30**, 1910274 (2020).
35. Wang, Y. Y. *et al*. Recent progress on layered double hydroxides and their derivatives for electrocatalytic water splitting. *Adv. Sci*. **5**, 1800064 (2018).
36. Meng, L. J. et al. Anomalous thickness dependence of Curie temperature in air-stable two-dimensional ferromagnetic 1T-$CrTe_2$ grown by chemical vapor deposition. *Nat. Commun*. **12**, 809 (2021).
37. Shi, S. Y. et al. All-electric magnetization switching and Dzyaloshinskii–Moriya interaction in $WTe_2$/ferromagnet heterostructures. *Nat. Nanotechnol*. **14**, 945-949 (2019).
38. Gambardella, P. *et al*. Ferromagnetism in one-dimensional monatomicmetal chains. *Nature* **416**, 301-304 (2002).
39. Tong, W. M. *et al*. Electrolysis of low-grade and saline surface water. *Nat. Energy* **5**, 367-377 (2020).
40. Yu, J. et al. Seawater electrolyte-based metal-air batteries: from strategies to applications. *Energy Environ. Sci*. **13**, 3253-3268 (2020).
41. Wang, Q. C. *et al*. Pyridinic-N-dominated doped defective graphene as a superior oxygen electrocatalyst for ultrahigh-energy-density Zn-air batteries. *ACS Energy Lett*. **3**, 1183-1191 (2018).
42. Chen, R. *et al*. Layered structure causes bulk NiFe layered double hydroxide unstable in alkaline oxygen evolution reaction. *Adv. Mater*. **31**, 1903909 (2019).
43. Kresse, G. *et al*. Ab initio molecular dynamic for liquid metals. *Phys. Rev. B* **47**, 558 (1993).
44. Kresse, G. *et al* . From ultrasoft pseudopotentials to the projector augmented-wave method. *Phys. Rev. B* **59**, 1758 (1999).
45. Blöchl, P. E. Projector augmented-wave method. *Phys. Rev. B* **50**, 17953 (1994).
46. Perdew, J. P. *et al*. Gneralized gradient approximaion made simple. *Phys. Rev. Lett.* **77**, 3865 (1996).
47. Dudarev, S. L. *et al*. Electron-energy-loss spectra and the structural stability of nickel oxide: an LSDA+U study. *Phys. Rev. B* **57**, 1505 (1998).
48. Andriotis, A. N. *et al*. Tunable magnetic properties of transition metal doped $MoS_2$. *Phys. Rev. B* **90**, 125304 (2014).
49. Mishra, R. *et al*. Long-range ferromagnetic ordering in manganese-doped two-dimensiaonal dichalcogenides. *Phys. Rev. B* **88**, 144409 (2013).
50. Tang, W. *et al*. A grid-based Bader analysis algorithm without lattice bias. *J. Phys.: Condens. Matter.* **21**, 084204 (2009).

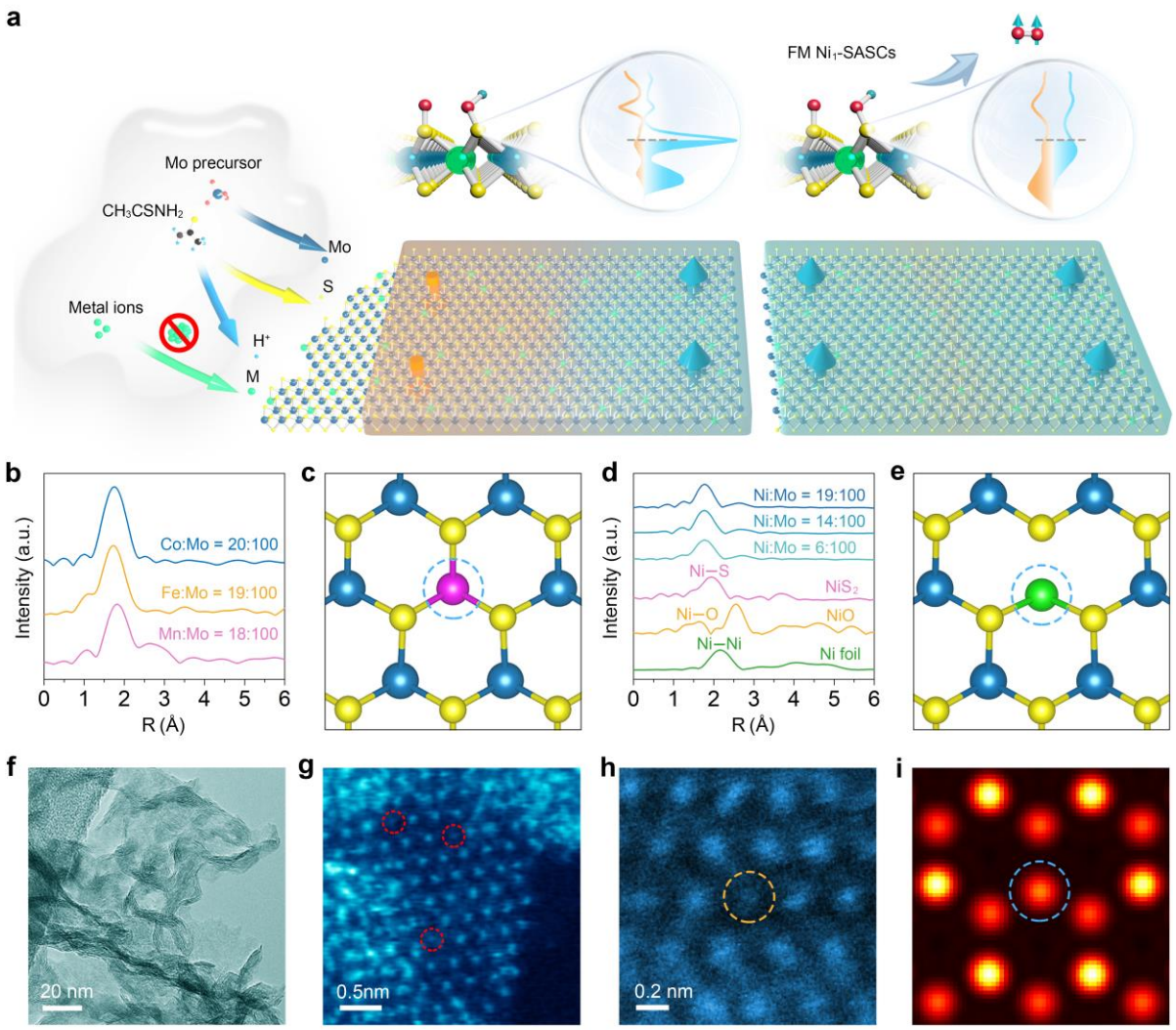


**Fig. 1 | Synthesis and characterization of a series of $M_1/MoS_2$ SASCs. a**, Illustration of the hydrothermal synthesis of $M_1/MoS_2$ SASCs under acidic conditions and the giant magnetic field enhancement of ferromagnetic SASCs for water splitting. **b**, Metal dopant K-edge FT-EXAFS spectra of $M_1/MoS_2$ ($Mn_1$, $Fe_1$, $Co_1$). **c**, Trigonal prismatic geometry of $M_1/MoS_2$ ($Mn_1$, $Fe_1$, $Co_1$). **d**, Ni K-edge FT-EXAFS spectra of $Ni_1/MoS_2$ SASCs with different Ni contents and the reference samples. **e**, distorted tetragonal structure of $Ni_1/MoS_2$. Yellow, blue and green spheres denote S, Mo and Ni atoms, respectively. **f**, TEM image of $Ni_1/MoS_2$. **g**, STEM image of $Ni_1/MoS_2$ resolves a characteristic triangular lattice consisting of brighter and darker sites (red circle), which can be assigned to Mo and Ni atomic sites, respectively. **h**, A zoom-in HAADF-STEM image of a single $Ni_{Mo}$ site (marked by yellow circle) with a darker contrast. **i**, The simulated HAADF-STEM image of DFT-optimized $Ni_{Mo}$ structure.

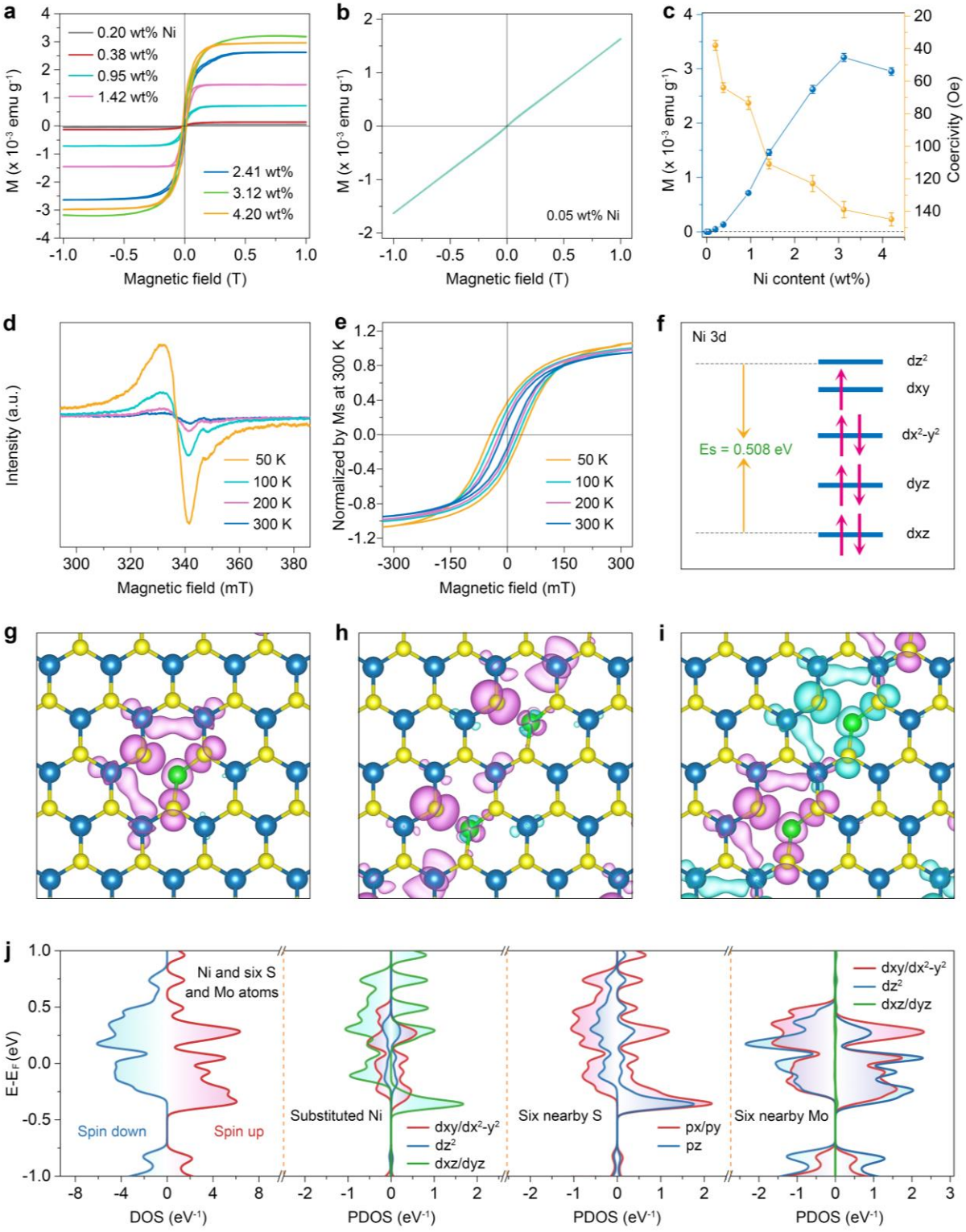


**Fig. 2 | Ferromagnetism of $Ni_1/MoS_2$. a**, Magnetization curves (M-H) of ferromagnetic $Ni_1/MoS_2$ with different Ni contents at 300 K. (Ni:Mo = 0.8:100, 1.6:100, 4:100, 6:100, 10:100, 14:100, 19:100). **b**, M-H curve of $Ni_1/MoS_2$ with extremly low loadig of 0.05 wt% Ni (Ni:Mo = 0.2:100). **c**, The staurated magnetization and coercivity of $Ni_1/MoS_2$ with different

Ni contents at 300 K. **d**, Temperature-dependent electron spin resonance (ESR) spectra of $Ni_1/MoS_2$ (14:100). **e**, Temperature-dependent M-H curves of $Ni_1/MoS_2$ (14:100). **f**, *d*-orbital spliting of a $Ni_{Mo}$ site with the distorted tetragonal gemetry. **g-i**, Spin density plots of (**g**) a single $Ni_{Mo}$ site, two adjacent $Ni_{Mo}$ sites with (**h**) ferromagnetic and (**i**) antiferromagnetic coupling. **j**, Total and projectecd DOS of individal $Ni_{Mo}$ site with neighboring six S and Mo atoms in ferromagnetic $Ni_1/MoS_2$ as shown in **Fig. 2h**. Yellow, blue and green spheres denote S, Mo and Ni atoms, respectively. The light blue and purple isosurfaces represent the spin-up and spin-down of $Ni_1/MoS_2$, respectively.

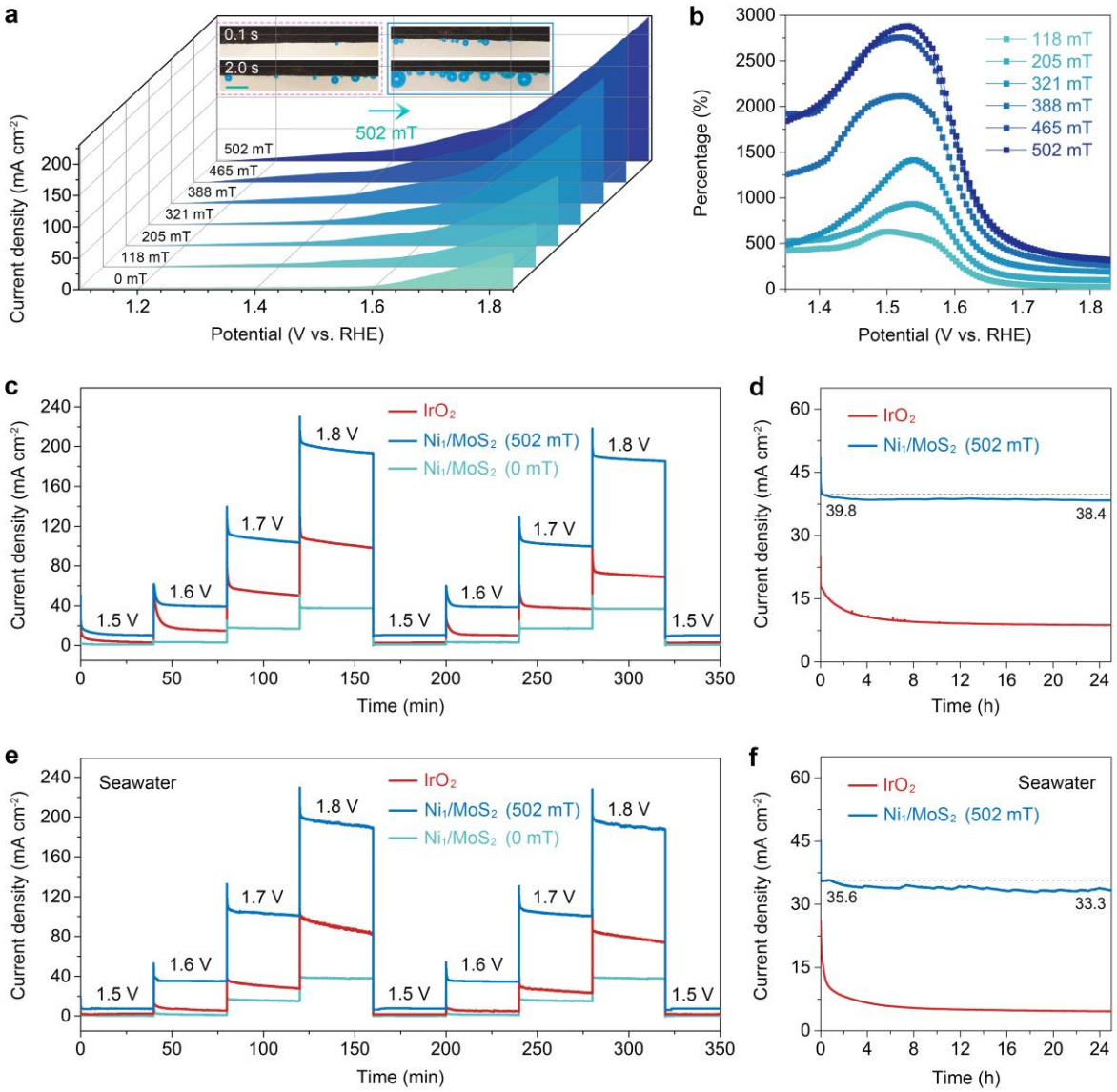


**Fig. 3 | Giant MEF of ferromagentic $Ni_1/MoS_2$ for OER and wafer splitting. a**, LSV curves of $Ni_1/MoS_2$ under different magnetic fields. Inset: Photo images of $Ni_1/MoS_2$ as OER catalysts in water splitting cells at 1.65 V without (left) and with (right) magnetic fields. The oxygen bubbles formed on catalyst surface are highlighted with blue false color for visual guidance. Scale bar: 100 μm. **b**, Giant MFE of $Ni_1/MoS_2$ with dramatically increaesd magnetocurrent density for OER. **c**, Current density plot of $IrO_2$ and $Ni_1/MoS_2$ at 1.5-1.8 V before and after applying a magnetic field of 502 mT in water splitting cells. **d**, I-T curves of $Ni_1/MoS_2$ under the magentic field to comapre with that of $IrO_2$ catalyst in water splitting cells. **e**, Current density plot of $IrO_2$ and $Ni_1/MoS_2$ at 1.5-1.8 V before and after applying a magnetic field of 502 mT in seawater splitting cells. **f**, I-T curves of $Ni_1/MoS_2$ under the magentic field to comapre with that of $IrO_2$ catalyst in seawater splitting cells.

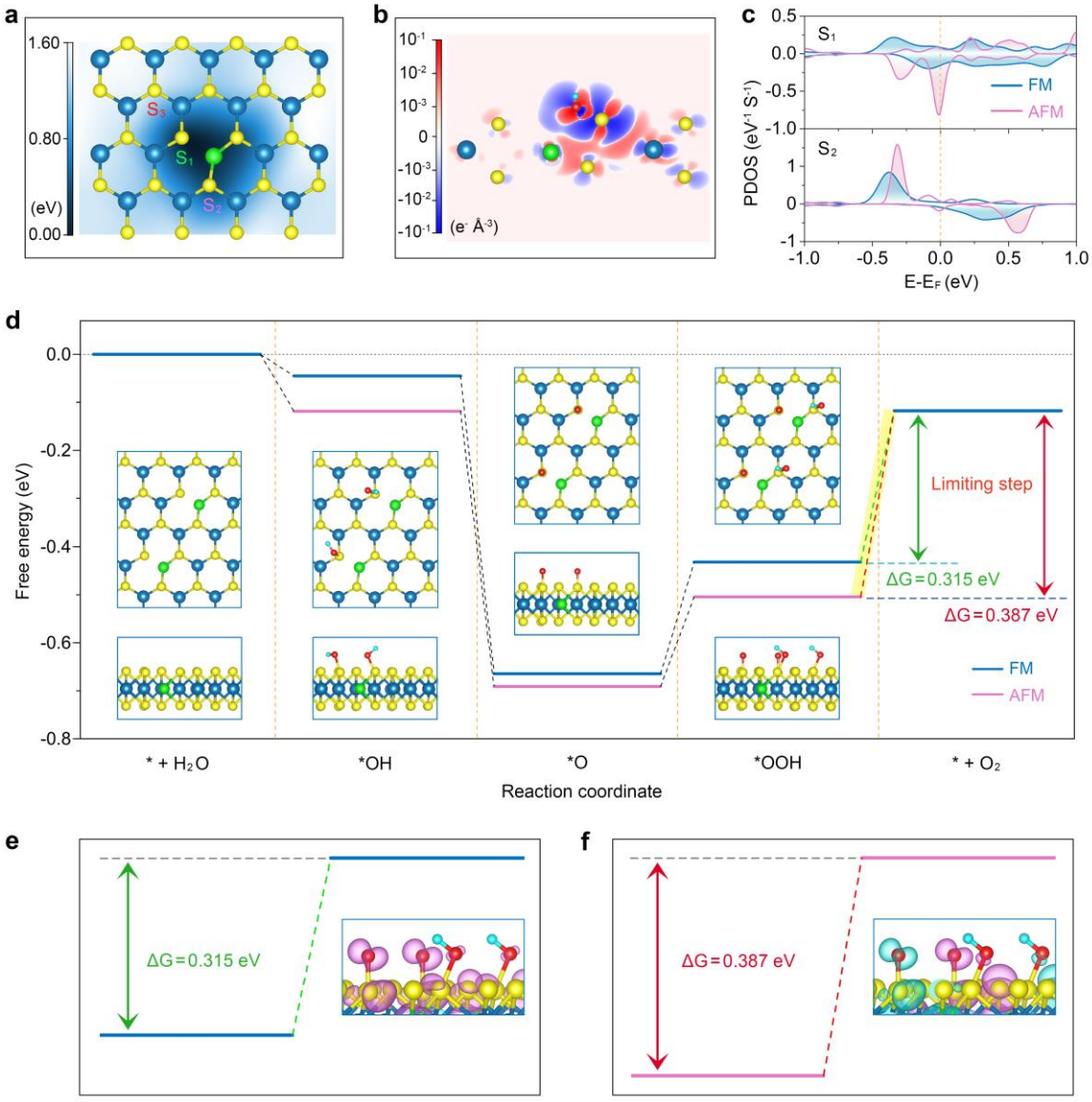


**Fig. 4 | The origin of giant MEF of ferromagentic $Ni_1/MoS_2$. a**, Adsorption energy contour map of a single *OH on the $Ni_{Mo}$ region, three different S sites are labeled as $S_1$, $S_2$, $S_3$ respectively. **b**, The corresponding charge difference density of a single $Ni_{Mo}$ site upon the adsorption of *OH. **c**, PDOS of $S_1$ and $S_2$ atoms of $Ni_1/MoS_2$ models (shown in **d**) consisting two ajdacent $Ni_{Mo}$ sites with ferromagnetic (dark blue) and antiferromagnetic (pink) coupling. **d**, Free energy profile of OER with the correpsonnding adsorption configurations of reaction intermedaites over ferromagnetic (dark blue) and antiferromagnetic (pink) $Ni_1/MoS_2$. **e**, **f**, The spin density plot of *OOH on S site over ferromagnetic (**e**) and antiferromagnetic (**f**) $Ni_1/MoS_2$ model towards the transition from *OOH to $O_2$. The light blue and purple isosurfaces represent the spin-up and spin-down, respectively.

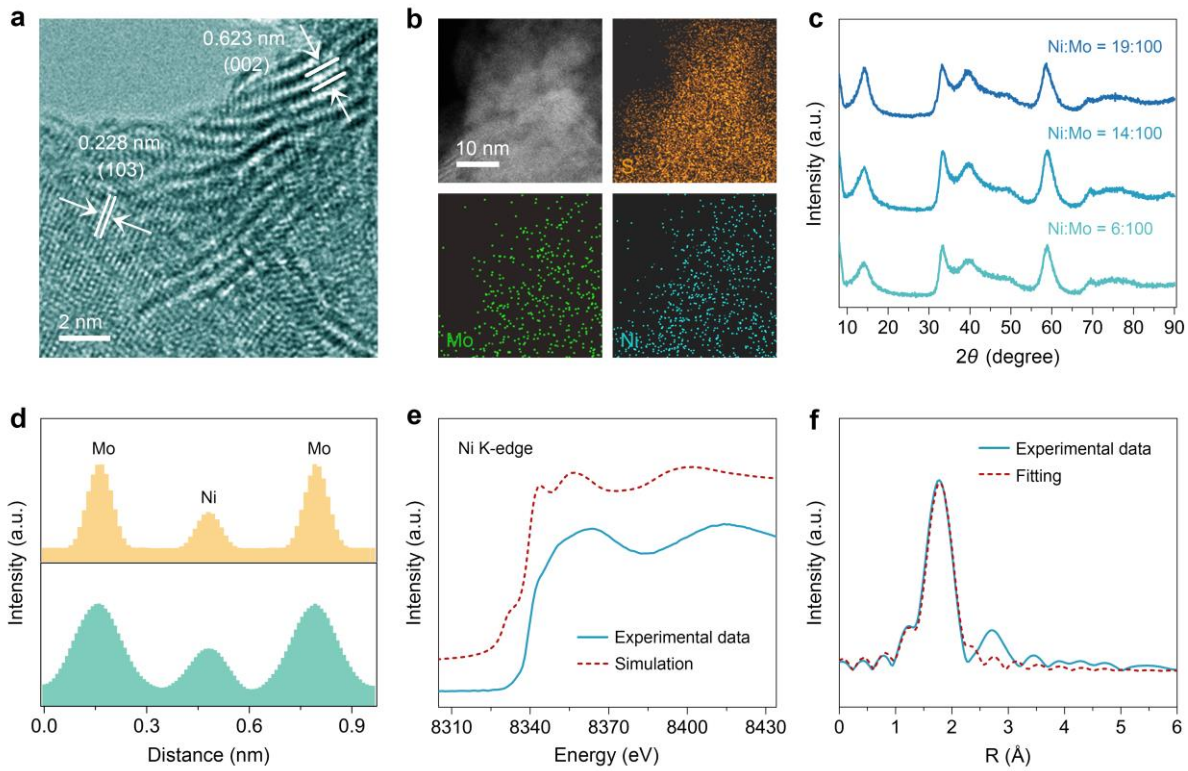


**Extended Data Fig. 1 | Structural characterization of $Ni_1/MoS_2$ with different metal loading. a**, HRTEM image of $Ni_1/MoS_2$ (14:100). **b**, HAADF-STEM image and corresponding EDS maps of $Ni_1/MoS_2$ (14:100). **c**, XRD patterns of $Ni_1/MoS_2$ with different Ni contents. **d**, The experimental (green) linear intensity profile of STEM (**Fig. 1h**) and the calculated data (**Fig. 1i**) (yellow) of $Ni_1/MoS_2$. **e**, The experimental (solid line) and theoretical(dotted line) curves of Ni K-edge XANES spectra. **f**, The FT- EXAFS function (solid line) and the result of fitting (dotted line) of the first Ni-S shell in the real-space.

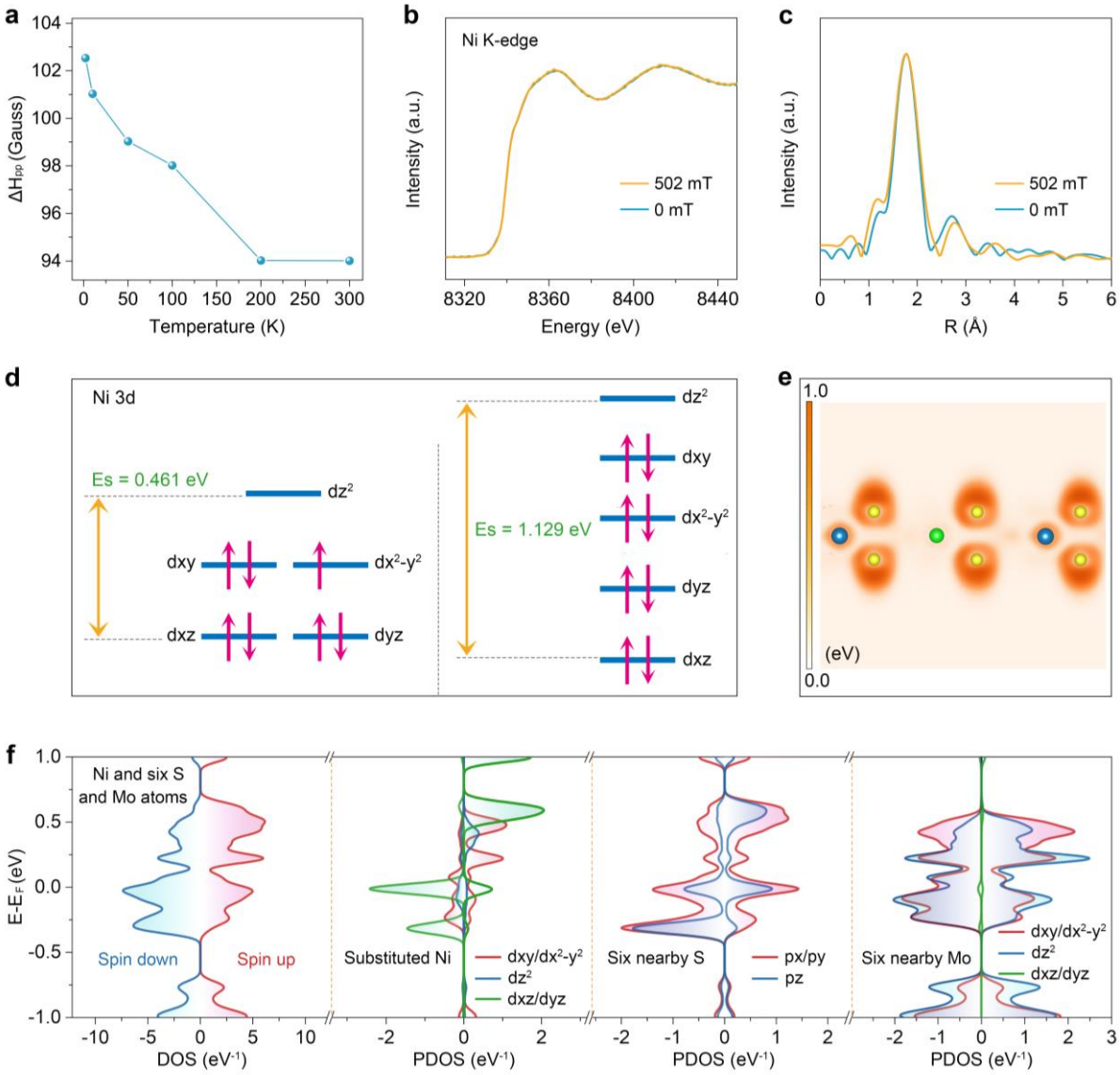


**Extended Data Fig. 2 | Characterization and the origin of ferromagnetism in $Ni_1/MoS_2$.** **a**, The peak seperation of ESR spectra for $Ni_1/MoS_2$ (14:100) under different temperatures. **b**, **c**, Comparison of the Ni K-edge XANES (**b**) and FT-EXAFS (**c**) spectra for $Ni_1/MoS_2$ (14:100) with and without applied magnetic field. **d**, *d*-orbtial spliting of a $Ni_{Mo}$ site for six (left, Es = 0.461 eV, $C_{3h}$) and four (right, Es = 1.129 eV, $C_{2v}$) coordination numbers. **e**, The energy localized function (ELF) of one Ni dopant-substituted Mo site in $MoS_2$. **f**, Total and projected DOS of individual $Ni_{Mo}$ site with neighboring six S and Mo atoms in antiferromagnetic $Ni_1/MoS_2$ as shown in **Fig. 2i**. Yellow, blue and green spheres are S, Mo and Ni atoms, respectively.

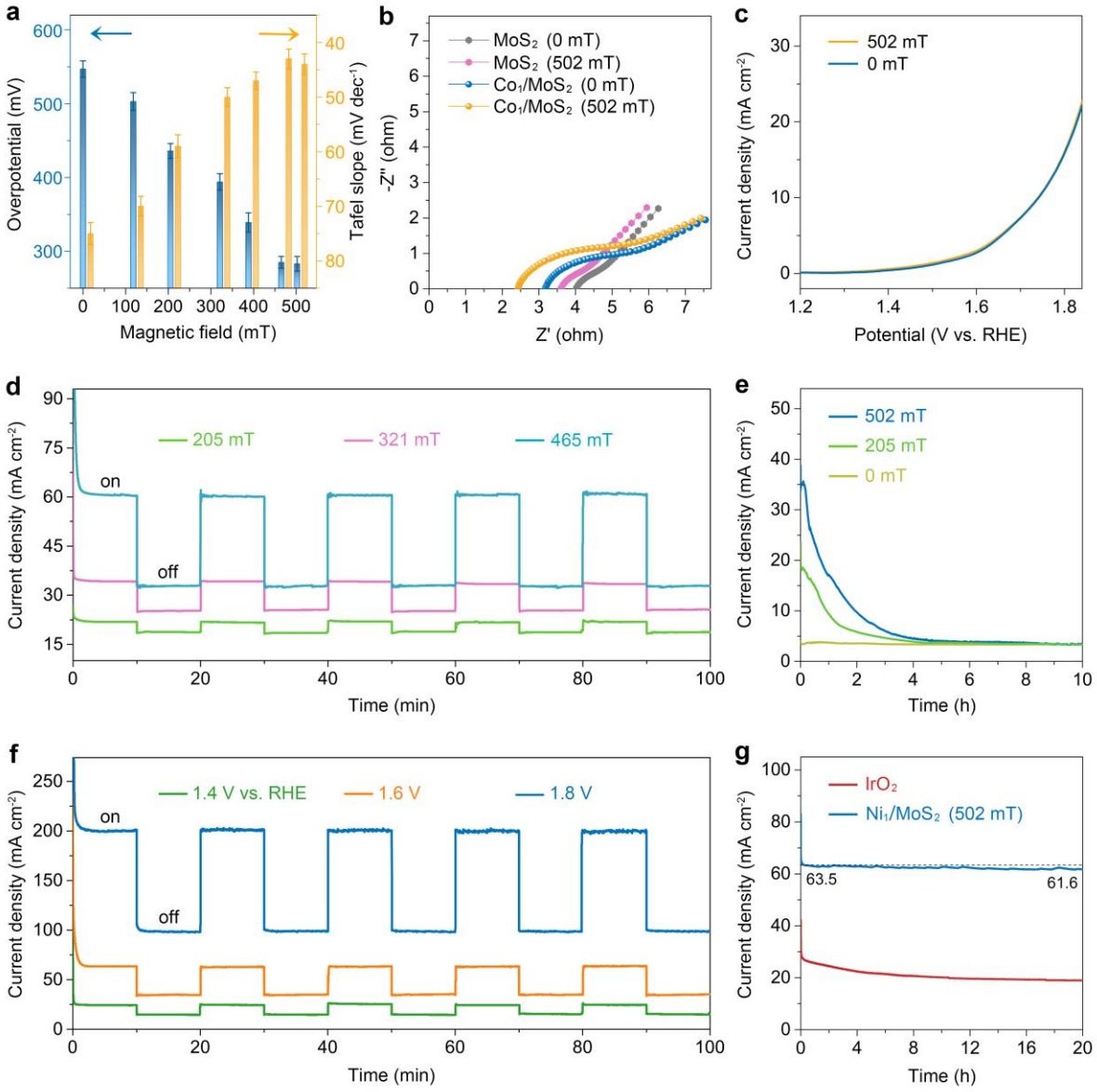


**Extended Data Fig. 3 | MFE of $Ni_1/MoS_2$ for OER and the comparison with commercial $IrO_2$ catalysts. a**, Overoptentials of $Ni_1/MoS_2$ (14:100) at current density of 40 mA $cm^{-2}$ and Tafel slopes. **b**, EIS spectra of $MoS_2$ and $Co_1/MoS_2$ with and withot magnetic field. **c**, LSV curves of $Ni_1/MoS_2$ (0.8:100). **d**, I-T curves of $Ni_1/MoS_2$ upon switching on and switching off different magnetic fields at 1.6 V vs. RHE. **e**, I-T curves of $Ni_1/MoS_2$ after switching off magnetic fields at 1.6 V vs. RHE. **f**, I-T curves of $Ni_1/MoS_2$ at different voltages upon switching on and switching off the magnetic field at 502 mT. **g**, I-T curves of $Ni_1/MoS_2$ under 502 mT and $IrO_2$ catalyst at 1.6 V vs. RHE.

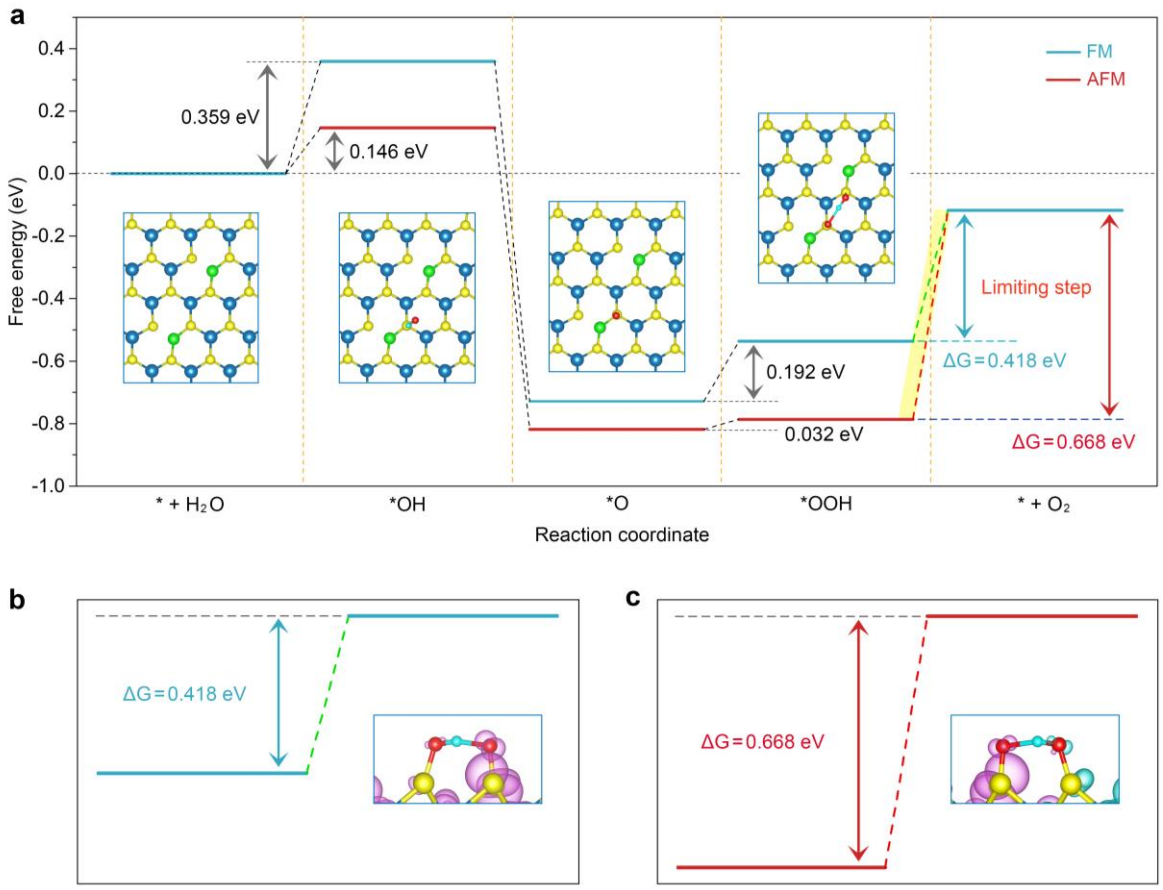


**Extended Data Fig. 4 | The origin of giant MEF of ferromagentic $Ni_1/MoS$. a**, The second possible free energy profile of OER with the corresponding adsorption configurations of reaction intermediates over ferromagnetic (cyan) and antiferromagnetic (dark red) $Ni_1/MoS_2$. **b**, **c**, The spin density plot of *OOH on S site over ferromagnetic (**b**) and antiferromagnetic (**c**) $Ni_1/MoS_2$ model towards the transition from *OOH to $O_2$. Yellow, blue, green, red and light blue spheres are S, Mo, Ni, O and H atoms, respectively. The light blue and purple isosurfaces represent the spin-up and spin-down density, respectively.

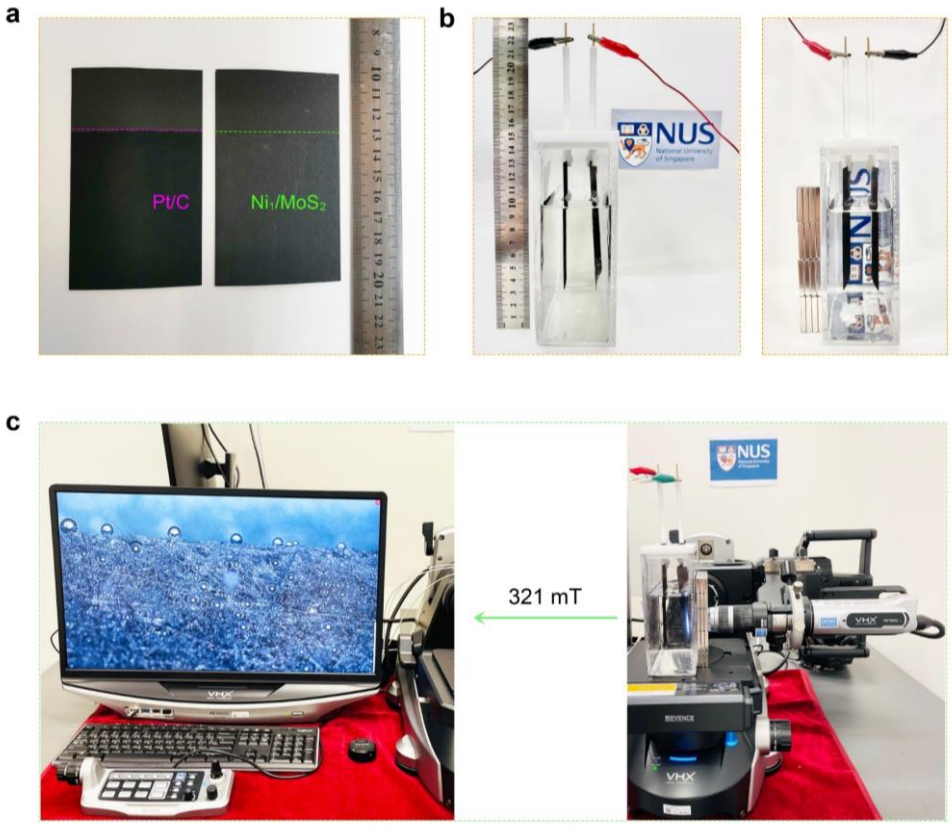


**Extended Data Fig. 5 | Giant MFE of 2.4 inch-sized ferromagnetic $Ni_1/MoS_2$ (14:100) electrode for a large water splitting cell. a**, Photograph of the inch-sized $Ni_1/MoS_2$ and Pt/C electrodes. **b-c**, inch-sized $Ni_1/MoS_2$ as anode (**b**) for magnetic-field enhanced water splitting (**c**).